Manuscript prepared for Biogeosciences Discuss.
with version 2.2 of the LaTeX class copernicus_discussions.cls.
Date: 8 November 2011

Filling-in of broad far-red solar lines by terrestrial fluorescence and atmospheric Raman scattering as detected by SCIAMACHY satellite measurements

J. Joiner[1], Y. Yoshida[2], A. P. Vasilkov[2], E. M. Middleton[1], P. K. E. Campbell[3], Y. Yoshida[4], A. Kuze[5], and L. A. Corp[6]

[1]NASA Goddard Space Flight Center, Greenbelt, MD, USA
[2]Science Systems and Applications, Inc., 10210 Greenbelt, Rd., Ste 400, Lanham, MD, USA
[3]University of Maryland, Baltimore County, Joint Center for Environmental Technology (UMBC-JCET), Baltimore, MD, USA
[4]National Institute for Environmental Studies (NIES), Tsukuba-City, Ibaraki, Japan
[5]Japan Aerospace Exploration Agency (JAXA), Tsukuba-City, Ibaraki, Japan
[6]Sigma Space Corp., Lanham, MD USA

Correspondence to: J. Joiner (joanna.joiner@nasa.gov)

Abstract

Global mapping of terrestrial vegetation fluorescence from space has recently been accomplished with high spectral resolution ($\nu/\Delta\nu > 35000$) measurements from the Japanese Greenhouse gases Observing SATellite (GOSAT). These data are of interest because they can potentially provide global information on the functional status of vegetation including light use efficiency and global primary productivity that can be used for global carbon cycle modeling. Quantifying the impact of fluorescence on the O_2-A band is important as this band is used for cloud- and aerosol-characterization for other trace-gas retrievals including CO_2. Here, we demonstrate that fluorescence information can be derived from space using potentially lower-cost hyperspectral instrumentation, i.e., more than an order of magnitude less spectral resolution ($\nu/\Delta\nu \sim 1600$) than GOSAT, with a relatively simple algorithm. As a demonstration, we use the filling-in of one of the few wide and deep solar Fraunhofer lines in the red and far-red chlorophyll-a fluorescence bands, the calcium II line near 866 nm, to retrieve fluorescence with the SCanning Imaging Absorption spectroMeter for Atmospheric CHartographY (SCIAMACHY) satellite instrument. Although the signal from vegetation fluorescence is extremely weak at 866 nm, our results suggest that useful information may be obtained after adjustments are made to the observed spectra to correct for instrumental artifacts. We compare fluorescence from SCIAMACHY with that retrieved at 758 and 770 nm from similarly-corrected GOSAT data as well with the Enhanced Vegetation Index (EVI) from the MODerate-resolution Imaging Spectroradiometer (MODIS). We also show that filling-in occurs at 866 nm over barren areas, possibly originating from luminescent minerals in rock and soil.

1 Introduction

Fluorescence from terrestrial vegetation has been measured in the laboratory and with ground- and aircraft-based instruments for several decades (see e.g., the review of

Meroni et al., 2009, and the many references therein). More recently, it has been demonstrated that fluorescence information can also be derived from satellite passive sensors measuring backscattered sunlight at red and far-red wavelengths. These fluorescence measurements, particularly with global coverage from satellites, are of interest because the signal originates from the core complexes of the photosynthetic machinery where energy conversion of absorbed photosynthetically active radiation occurs. Chlorophyll fluorescence measurements therefore provide a means to estimate global instantaneous vegetation carbon-related processes. These processes are of major interest for precision farming, forest management, and assessment of the terrestrial carbon budget including gross primary productivity (GPP) (e.g., Campbell et al., 2008; Damm et al., 2010; Frankenberg et al., 2011b). In addition, it is important to quantify the impact of fluorescence on atmospheric absorption bands, such as the O_2-A band, that are used for cloud- and aerosol-characterization for other trace-gas retrievals including CO_2 (Frankenberg et al., 2011a).

Fluorescence in vegetation occurs because a portion of the sunlight absorbed by chlorophyll cannot be used for carbon fixation. While most of this unused energy is given off as heat, a small fraction is re-emitted as fluorescence at longer wavelengths (lower energy) with respect to the excitation wavelength. The far-red and red fluorescence generally occurs as a convolution of broad band emission with two peaks at 685 and 740 nm, respectively, as shown in Fig. 1 (e.g., Meroni et al., 2009; Corp et al., 2003, 2006). Most studies have shown that in high light conditions (i.e., in the afternoon when GOSAT measurements are made) and when plants are under stress, fluorescence is correlated with photosynthesis and light use efficiency (LUE) (e.g., Flexas et al., 2002; Louis et al., 2005; Meroni et al., 2008; van der Tol et al., 2009; Zarco-Tejada et al., 2009; Amoros–Lopez et al., 2008). Variations in fluorescence and photosynthesis occur when protective mechanisms intervene to prevent damage by harmful radicals that are formed under these conditions.

Several studies have indicated that chlorophyll fluorescence supplies information content that is complementary to reflectance-based spectral vegetation indices includ-

ing the Normalized Difference Vegetation Index (NDVI) and Enhanced Vegetation Index (EVI), related to chlorophyll content, and the Photochemical Reflectance Index (PRI), related to changes in xanthophyll cycle pigments (Meroni and Colombo, 2006; Middleton et al., 2008; Rascher et al., 2009; Middleton et al., 2009). For example, Guanter et al. (2007) showed satellite observations with low variation of the NDVI within a field, while PRI and fluorescence (F_s) showed significant variations. PRI and F_s were not correlated, perhaps owing to the large dependence of PRI on the canopy structure. Zarco-Tejada et al. (2009) similarly showed no correlation between crown fluorescence and NDVI measured from airborne imagery. Meroni et al. (2008) showed that F_s normalized by incoming photosynthetically active radiance (PAR) was correlated with LUE regardless of stress, while PRI showed a more complex relationship. Preliminary results from Joiner et al. (2011a) showed that fluorescence derived from satellite measurements in some areas appears to lead EVI/NDVI by a month or so during green up and brown down periods. Both Joiner et al. (2011a) and Frankenberg et al. (2011b) showed areas and vegetation types for which fluorescence and vegetation indices differed, particularly moderate to high latitude evergreen that maintains its pigment during winter inactivity.

Space-based measurement of solar-induced chlorophyll fluorescence is challenging, because its signal (typically 1–5% red and far-red wavelengths) is small as compared with the much larger reflectance signal. Ground- and aircraft-based approaches have made use of the dark and spectrally-wide O_2-A ($\sim$760 nm) and O_2-B ($\sim$690 nm) atmospheric features to detect the weak fluorescence signal (see e.g., Meroni et al., 2009). Deep solar Fraunhofer lines have also been used to detect fluorescence from vegetation using airborne and ground-based sensors. Initial studies (e.g., Plascyk and Gabriel, 1975; McFarlane et al., 1980; Watson, 1981; Sioris et al., 2003) focused on lines shortward of the red edge ($\sim$700nm) where the terrestrial surface albedo is relatively low. More recently, Joiner et al. (2011a) and Frankenberg et al. (2011a,b) focused on longer-wavelength solar Fraunhofer lines that can be observed with space-based instruments such as the currently operational GOSAT and the upcoming OCO-2. They

showed that fluorescence can be detected using Fraunhofer lines away from the chlorophyll fluorescence peak even when the surface is relatively bright.

Here, we build on that work making use of unique spectral measurements from the SCanning Imaging Absorption spectroMeter for Atmospheric CHartographY (SCIAMACHY) instrument aboard the European Space Agency (ESA) Environmental satellite (EnviSat). Spectral radiance measurements encompassing a wide solar Fraunhofer calcium (Ca) II line at 866 nm are used to retrieve an additive signal that fills in the line. These measurements are at the long wavelength tail of the chlorophyll-a fluorescence spectrum.

Very few laboratory and ground-based measurements of vegetation fluorescence have been reported at wavelengths longer than 800 nm. Figure 1 displays measurements acquired using polychromatic excitation at wavelengths shorter than 665 nm with a so-called solar simulator after a five minute dark adaptation of the samples as described in Campbell et al. (2008). Chlorophyll fluorescence levels decrease significantly from the dark-adapted maximum (F_{max}) to the steady state (F_s) in 15–20 s, after which they remain relatively constant. Here, we show that F_{max} and F_s in the red and far-red peaks varies significantly, while similar and much lower values occur at the fluorescence spectrum tails (e.g., at 656 and 854-866 nm). Amoros–Lopez et al. (2008) similarly report spectral measurements from 650-850 nm showing a small amount of fluorescence ($\sim$0.1 mW/m^2/nm/sr) at the longest wavelength when illuminated by sunlight through a filter at wavelengths shorter than about 600 nm (i.e., not full ambient intensity at leaf level). Other measurements (e.g., Chappelle and Williams, 1987; Rosema et al., 1991; Edner et al., 1994; Saito et al., 1998) suggest that the tail of the chlorophyll-a fluorescence bands and perhaps fluorescence from other compounds such as vitamin K_1 (Chappelle et al., 1984) may produce a measurable signal at wavelengths beyond 800 nm. Measurements have shown that the excitation efficiency of chlorophyll fluorescence is high in the blue and ultraviolet (UV) with a minimum around 550 nm and another peak of high efficiency beyond about 650 nm (Chappelle and Williams, 1987; Rosema et al., 1991; Middleton et al., 2008). Therefore, solar-induced

fluorescence at long wavelengths may be higher than that measured by laser or in a partially-illuminated scenario.

In addition to vegetation, minerals in rocks and soil may luminesce from blue to far-red wavelengths and contribute to the filling-in of Fraunhofer lines. Mineral detection was a primary goal of early measurements using the Fraunhofer line discriminator method (e.g., Hemphill and Vickers, 1966; Watson, 1981; Stacy et al., 1984; Hemphill et al., 1988). For example, Watson (1981) found that luminescence at 489 nm from an airborne Fraunhofer line discriminator instrument had a good correlation with fluorite concentrations measured in soil samples collected along two traverses.

A primary objective of this work is to explore the possibility of making fluorescence measurements from space with lower spectral resolution instrumentation than either the GOSAT interferometer or the OCO-2 spectrometer. If this can be demonstrated, then low cost instrumentation can potentially be used for such measurements with a relatively simple retrieval algorithm, i.e., one that does not require complex atmospheric correction. Of the wide and deep solar lines shown in Fig. 1, we focus on the 866 nm Ca II solar Fraunhofer line, because it is the only line with negligible contamination from atmospheric water vapor capable of detecting fluorescence at spectral resolutions of about 0.5 nm. However, this is clearly not an optimal wavelength region for measuring fluorescence owing to the weakness of the signal; instrumental artifacts can easily overwhelm the fluorescence signal. SCIAMACHY is the only satellite instrument making hyperspectral measurements at 866 nm. Though not optimized for detecting fluorescence, it can be used for an exploratory study.

The paper is organized as follows: Sect. 2 describes the satellite observations used here. Simulations of the Ca II line-filling at 866 nm from atmospheric rotational- and vibrational-Raman scattering as well as chlorophyll fluorescence are given in Sect. 3. The details of our retrieval approach, including methodology to correct for instrumental artifacts, are provided in Sect. 4. We show maps of monthly-mean fluorescence derived from 866 nm Ca II line-filling and a seasonal climatology derived from more than 8 years of SCIAMACHY data in Sect. 5. In this section, we also compare and contrast

temporal and spatial variations of fluorescence (retrieved from both SCIAMACHY and GOSAT) and the MODIS enhanced vegetation index (EVI). Conclusions are given in Sect. 6.

2 Satellite observations

2.1 SCIAMACHY

SCIAMACHY is a grating spectrometer that measures transmitted, reflected, and scattered sunlight in both limb- and nadir-viewing geometries from ultraviolet to near-infrared wavelengths (212–2386 nm) in eight separate channels. It was launched on the EnviSat platform in February 2002 into a sunsynchronous orbit with a descending node equator crossing time near 10:00. The instrument can make measurements in a number of different modes (e.g. Lichtenberg et al., 2006). In addition to Earth views in the limb and nadir, it can operate in a solar or lunar occultation mode. It also measures the solar irradiance. In this work, we primarily use channel 5 that covers wavelengths between 773 and 1063 nm at a spectral resolution of 0.54 nm. The signal-to-noise ratio for nadir measurements in this channel is between 1000 and 10000 (Gottwalk et al., 2006). We also examined spectra in channel 4 that covers 595-812 nm at 0.48 nm spectral resolution.

We processed raw SCIAMACHY level 1B data with the SciaL1c command-line tool software package (DLR, 2006). Using this package, we applied all available corrections and calibrations. Although the corrections do an excellent job of removing most artifacts that produce false filling-in of solar Fraunhofer lines, we found it necessary to further account for the remaining effects as discussed in Sect. 4. In App. A, we give a brief overview of the effects. More details can be found in Lichtenberg et al. (2006).

2.2 GOSAT

GOSAT is a satellite mission designed to monitor the global distribution of the greenhouse gases CO_2 and CH_4 (Yokota et al., 2009). Jointly developed by the Japanese Ministry of the Environment (MOE), the National Institute for Environmental Studies (NIES), and the Japanese Aerospace Exploration Agency (JAXA), GOSAT was launched on 23 January 2009 into a sun-synchronous orbit. It has a descending node equatorial crossing time near 13:00 LT and a 3 day repeat cycle. GOSAT has two instrument packages: 1) The Thermal And Near-infrared Sensor for carbon Observation-Fourier Transform Spectrometer (TANSO-FTS) (Kuze et al., 2009) that measures backscattered solar radiation in three shortwave infrared (SWIR) regions, referred to as "bands", centered at 0.76, 1.6, and 2.0 µm with a nadir ground footprint of 10.5 km diameter and 2) The Cloud and Aerosol Imager (CAI) that contains four bands at 0.38, 0.67, 0.87, and 1.6 µm and footprints between 0.5 and 1.5 km.

Joiner et al. (2011a) and Frankenberg et al. (2011b) retrieved chlorophyll fluorescence using TANSO-FTS band 1. This band extends from approximately 758 to 775 nm with a resolving power ($\nu/\Delta\nu$) of > 35000. The signal-to-noise ratio (SNR) for this band is > 300 for a typical scene radiance.

There are also instrumental effects that can distort GOSAT spectra to produce a false filling-in of Fraunhofer lines. These include non-linearity from the analog-to-digital converter (ADC) (Kuze et al., 2011b) and the analog filter circuit in band 1 that can lead to effects such as a zero-level offset (Frankenberg et al., 2011b). In addition, calibration drift (Kuze et al., 2011a) may produce errors and drift in the absolute values of derived fluorescence. The latest available version (v130) of the level 1b data addresses some, but not all of these problems. Future versions will provide more corrections for these non-linearities. Only a limited amount of v130 data is currently available. Therefore, here we use a previous version of level 1b data (v050) with an approach to account for instrumental artifacts that produce false filling in as described below.

2.3 MODIS Vegetation indices

Below, we compare satellite-derived fluorescence with the Enhanced Vegetation Index (EVI) (Huete et al., 2002), a popular vegetation reflectance-based index that indicates relative greenness and is used to infer photosynthetic function. The EVI, derived from the MODIS instrument, can be found in the "Vegetation Indices 16-Day L3 Global 1km" (MOD13A2) data set. We use data from the Aqua MODIS exclusively here. The Aqua satellite has an ascending node equator crossing near 13:30 LT, similar to that of GOSAT. Although these data have been cloud-filtered and corrected for aerosol-corruption effects, we followed the methodology of Xu et al. (2011) to further remove residual atmospheric corruption in order to produce the best possible signals from vegetation.

3 Simulated filling-in at 866 nm

Here, we simulate the effects of fluorescence as well as rotational- and vibration-Raman scattering on space-based observations of the Ca II line near 866 nm. We use the so-called KPNO2010 high spectral resolution solar irradiance reference spectrum (Chance and Kurucz, 2010) for these simulations and convolve the spectrum with triangular instrument line shape functions having different values of the full-width half-maximum (FWHM) including one similar to SCIAMACHY.

3.1 Fluorescence

Figure 2 shows simulated filling-in of the Ca II solar line at 866 nm for a spectrally constant fluorescence signal of 0.2 mW/m^2/sr/nm for several different spectral resolutions including the limit at monochromatic resolution. Because Rayleigh optical thickness is low at these wavelengths, we did not include atmospheric scattering in these simulations. The filling-in at SCIAMACHY resolution is small ($<$1%). However, modest increases in spectral resolution will increase the filling-in.

Figure 3 shows the surface-albedo dependence of the simulated filling-in of the Ca II line for the same amount of fluorescence (0.2 mW/m^2/nm/sr) and spectral resolutions as in Fig. 2. The surface albedo dependence is significant at low surface albedos. However, the dependence flattens out at values typical of vegetated land ($>\sim$0.25).

3.2 Rotational-Raman scattering

We computed the filling-in of the Ca II line due to rotational-Raman scattering (RRS) using the scalar Linearized Discrete Ordinate Radiative Transfer code (LIDORT-RRS) of Spurr et al. (2008). Figure 4 shows the filling-in of the Ca II line as in Fig. 2 but from rotational-Raman scattering (RRS) only. Although the amount of atmospheric scattering is relatively small at these wavelengths, the RRS filling-in is apparent owing to the large depth of this solar line as similarly shown by Joiner et al. (2011a) for the K I line at 770 nm. The spectral signature is very similar to that of line filling due to fluorescence. The filling-in due to RRS is about a factor of 6 less than that due to a fluorescence of 0.2 mW/m^2/nm/sr at SCIAMACHY resolution. This factor increases somewhat at higher spectral resolutions.

Figure 5 shows that the RRS filling-in dependence on surface albedo is relatively flat for albedos $>\sim$0.3. There is a small but significant dependence on both surface pressure and solar zenith angle (SZA). Figure 6 shows the SZA dependence in more detail as well as the dependence on satellite view zenith angle (VZA) and surface pressure. The SZA dependence is relatively small for SZA $< 60^\circ$, but increases rapidly for greater angles. The VZA dependence is small for typical angles viewed by SCIAMACHY.

3.3 Vibrational-Raman scattering

Vibrational Raman scattering (VRS) is commonly neglected in UV and visible retrieval algorithms as it is small compared with rotational-Raman scattering (RRS) (Burrows et al., 1996). However, the fractional contribution of VRS is larger in the near-InfraRed (NIR) owing to higher values of solar radiation at excitation wavelengths as compared

with emission wavelengths. The VRS frequency shifts between excitation and emission are $\Delta\nu \simeq$ 2331 and 1555 cm^{-1} for N_2 and O_2, respectively, assuming pure vibrational transitions of the molecules (Heise and Schrotter, 1995). We assessed the VRS contribution to the filling-in of the Ca II Fraunhofer line using the single scattering approximation of the radiative transfer equation. Along with photons only scattered in the atmosphere, we also accounted for photons first reflected from the surface and then scattered in the atmosphere.

Absolute differential Raman cross sections of the vibrational line at 488 nm at 90° measured by different authors for N_2 vary from 3.3×10^{-31} to 5.6×10^{-31} cm^2/str-mol (Fenner et al., 1973). Here, we use a value of 5.5×10^{-31} cm^2/str-mol that is consistent with data from Heise and Schrotter (1995). The ratio of O_2 to N_2 cross sections at 488 nm is assumed to be 1.3 (Fenner et al., 1973). We adopt a general form of phase functions for both the unshifted Cabannes line and wavelength shifted VRS lines as suggested by Danichkin et al. (1982). For the central Cabannes line in air, the depolarization ratio for unpolarized light is assumed equal to 0.00734 (Chance and Spurr, 1997). For VRS lines, we use values recommended by Danichkin et al. (1982), i.e., 0.043 and 0.099 for N_2 and O_2, respectively.

Figure 7 shows the VRS filling-in of the 866nm Ca II Fraunhofer line as a function of surface albedo. The maximum value of about 0.45% occurs for a non-reflecting surface. VRS filling-in rapidly decreases with increasing surface albedo. For typical values of surface albedo over land (> 0.2), the filling-in only weakly depends on surface albedo and does not exceed 0.02% for SZA$< 60°$. Therefore, we neglect VRS in the remainder of this study.

4 Retrieval methodology

4.1 Fitting windows

The use of solar Fraunhofer lines substantially simplifies a space-based retrieval of F_s as compared with the O_2-A band as described by Joiner et al. (2011a) and Frankenberg et al. (2011a); atmospheric correction is unnecessary as long as observations are made at wavelengths not affected by atmospheric absorption. Joiner et al. (2011a) used the potassium (K) I line near 770 nm to derive fluorescence using GOSAT's TANSO-FTS. This line falls between several weak O_2 lines and can be observed in relative isolation with GOSAT's high spectral resolution. Here, we derive fluorescence from GOSAT with the same fitting window used by Joiner et al. (2011a) (769.90–770.25 nm). We use a second fitting window between 758.45 and 758.85 nm and similar to Frankenberg et al. (2011b) scale the results from that window and add them to the other to increase the signal-to-noise ratio.

Of the solar lines shown in Fig. 1 (656, 850, 854, 866 nm), only the 866 nm Ca II line is relatively free of contamination by atmospheric water vapor absorption. We attempted fluorescence retrievals using all of these lines including the Hα line near 656 nm in SCIAMACHY channel 4. We found that it was extremely difficult to disentangle the fluorescence filling-in from water vapor absorption. Therefore, in the remainder of this work, we focus solely on deriving fluorescence using the 866 nm Ca II solar line from SCIAMACHY with the spectral band 863.5–868.5 nm.

4.2 General approach

We use a variation on the approach implemented by Joiner et al. (2011a) to jointly retrieve a reflectivity-related parameter K and an additive signal F_s presumably produced by some type of fluorescence. We use the above-mentioned spectra fitting windows with the following simplified model for the observed Earth spectral radiance $\boldsymbol{I}(\lambda)$ that

assumes negligible atmospheric absorption and scattering:

$$\boldsymbol{I}(\lambda) = K\boldsymbol{E}(\lambda)^* + F_s, \quad (1)$$

(Joiner et al., 2011a) where $\boldsymbol{E}(\lambda)^*$ is a reference spectrum containing no fluorescence.

As in Joiner et al. (2011a), we assume a constant wavelength dependence of F_s over our relatively small fitting windows. We fit both constant and linear in wavelength coefficients for K (i.e., $K = K_0 + K_1[\lambda - \lambda_0]$) for the larger SCIAMACHY fitting window, but only a constant for the smaller GOSAT window. The spectral dependence of atmospheric, cloud, and aerosol scattering is essentially constant over the relatively small narrow fitting windows used, so the neglect of it will have an insignificant effect on the retrieval of fluorescence. Similarly, calibration of the reference spectrum $E(\lambda)^*$ does not affect the derived fluorescence, since any offset between the reference and observed spectra is absorbed in the parameter K. An error in absolute calibration of $\boldsymbol{I}(\lambda)$, however, will produce an error in the retrieved F_s.

Similar to the approach of Joiner et al. (2011a), we use a standard weighted least squares fitting procedure. All wavelengths are weighted equally except for a few wavelengths within the GOSAT fitting window that are not used because they are affected by O_2 absorption.

4.3 Use of reference spectra

The main difference between our approach and that of Joiner et al. (2011a) is that we use spectral radiance measurements made over the cloudy ocean as a reference rather than a measured or computed solar irradiance spectrum. No further corrections to observed spectra are made. Our retrieval approach is insensitive to errors in the instrument line shape function or reference solar spectra as these are not used.

The main criterion for reference spectra used to derive terrestrial fluorescence is that they should represent the spectral shape of a solar Fraunhofer line without terrestrial fluorescence. There are several advantages of using cloudy Earth radiance spectra as a reference to derive the terrestrial fluorescence signal as opposed to solar irradiance

spectra (measured or computed). Firstly, the use of Earth spectra minimizes the so-called undersampling problem and eliminates errors due to inaccuracy of the assumed instrument line shape function. The undersampling problem and a proposed correction method have been discussed at length by Chance et al. (2005). However, we found that the proposed correction method did not achieve the desired accuracy owing to uncertainties in the instrument line shape function. Because the wavelength shifts are very small between ocean-based reference spectra and the land-spectra of interest, problems due to undersampling are essentially eliminated. Corrections used by Joiner et al. (2011a) to account for undersampling when referencing to observed solar spectra are not necessary.

Secondly, referencing to ocean spectra with similar continuum radiance values allows us to significantly reduce the errors from straylight, dark current, zero-level offset, and other instrumental effects described above that can produce a false filling-in. These effects should be present in the ocean reference spectra at approximately the same level. Therefore, the effects should be accounted for when deriving fluorescence using Eq. 1.

Finally, using ocean spectra at similar radiance levels and SZAs as a reference will also implicitly account for some of the filling-in due to RRS. RRS depends upon surface albedo as well as the mean pressure of the scattering surface. Here, we are using cloudy data at similar SZAs and continuum radiance values. Studies of the so-called optical centroid pressure (approximately, the reflectance-weighted mean pressure) of clouds over ocean at moderate reflectivities typical of vegetated land show that the clouds occur mainly between about 775 and 875 hPa (Joiner et al., 2011b). Deep convective and frontal clouds that have lower optical centroid pressures typically occur only at higher Lambertian-equivalent reflectivities ($>\sim$ 0.6). Therefore, the main difference in RRS filling-in between the cloudy ocean and land spectra is due to the different effective surface pressures. As shown in Fig. 5, this difference is small, but not negligible for the expected pressure differences. We must bear this difference in mind when examining our results. For regions with surface pressures higher than about

900 hPa, there may be unaccounted for filling-in due to RRS. However, for high-altitude land regions (< 775hPa) the reference ocean spectra may overestimate RRS filling-in.

Frankenberg et al. (2011b) used a different approach to account for instrumental artifacts; they utilized measurements over Antarctica to develop a parameterization for the false fluorescence produced by the zero-level offset in GOSAT data. They showed generally increasing amounts of false fluorescence with radiance levels with some wiggles and a downturn at the highest radiances in the S polarization. We found similar features using cloudy ocean data. With our approach, we are able to cover the full range of observed radiance values and see a downturn in the false fluorescence or filling-in at the highest radiance levels also in the P polarization. Our utilization of cloudy ocean data does not necessitate the use of high SZA data to cover the full range of observed continuum radiance values; filling-in from RRS increases rapidly at high SZAs as shown above, although the imprint of RRS is not obvious in the results of Frankenberg et al. (2011b).

Frankenberg et al. (2011b) discarded GOSAT P polarization data because the errors in that polarization were time-dependent. We likewise find such time-dependent errors in both GOSAT and SCIAMACHY data. Because cloudy ocean data are available year round, we are able to account for these errors and use all data including GOSAT P polarization, thereby significantly reducing the effects of instrumental noise.

In addition, cloudy ocean data span all latitudes. Therefore, we are able to account for instrumental effects that vary systematically with orbital phase; our approach is able to detect and correct for subtle but significant latitudinally-dependent artifacts in both GOSAT and SCIAMACHY data. We find that the latitudinal-dependence of these artifacts also varies with season.

Here, we binned potential reference spectra according to several criteria discussed below. For each bin, we averaged multiple spectra to produce a composite reference spectrum. To reduce any filling-in signal from the ocean, e.g., from ocean Raman scattering (Vasilkov et al., 2002), RRS, VRS, or fluorescence, we only use pixels with reflectances > 0.2 for SCIAMACHY. For GOSAT we used only pixels with a cloud frac-

tion (derived from the CAI) of $>$20%.

4.3.1 SCIAMACHY binning

For SCIAMACHY, we binned spectra separately for each of the two primary pixel exposure times and for each scan position within a nadir block according to the continuum radiance value and the wavelength shift (with respect to a fixed solar spectrum). We found that the observed filling-in over ocean sometimes changes abruptly and that it also drifts slowly over time. We therefore compute a set of reference spectra for each day of observations. If the standard deviation of the filling-in over ocean for a given day exceeds a threshold value, we eliminate that day from our sample.

We use a bin size of 0.1 for (normalized) radiance, represented by $R\cos(\mathrm{SZA})$ where R is the reflectance. We found that the wavelength shifts varied systematically with latitude, so binning by both wavelength shift and reflectivity implicitly accounts for filling-in features such as RRS that are function of solar zenith angle as well as instrumental artifacts that vary systematically with orbital phase. Because the wavelength shifts vary with time, we compute the daily mean and standard deviation of wavelength shift and use 8 bins with intervals of half the standard deviation of the wavelength shift (typically $\sim$0.007 nm).

4.3.2 GOSAT binning and additional corrections

For GOSAT, we used bin sizes of 0.05 for normalized radiance, 20° for latitude, and 0.001 nm for wavelength shift. We use only data processed with the H gain range as there are not enough data from the M range to perform a reliable correction. Therefore, data over the Sahara and in parts of central Australia have not been processed. For GOSAT, we retrieve F_s separately for the S and P polarizations (separate corrections applied) and combine them. We also apply a correction factor to the radiances to account for instrument degradation as suggested by Kuze et al. (2011a).

4.4 Cloud filtering

Because clouds do not alter the spectral structure used to retrieve F_s, we can tolerate small amounts of cloud within our satellite footprints; the main effect of clouds will be to shield a portion of the F_s signal from satellite view. We remove significantly cloud-contaminated data from our samples by two different methods. For SCIAMACHY, we use the concept of the cloud radiance fraction (CRF). CRF is defined as the fraction of pixel radiance scattered by cloud particles. The CRF is a convenient quantity for cloudy pixel screening, because it can be computed directly for large pixels and collocation with a subpixel imager is not necessary. The CRF is given by

$$\mathrm{CRF} = f\frac{I_{\mathrm{cld}}}{I_{\mathrm{obs}}}, \tag{2}$$

where f is the geometric cloud fraction, and I_{obs} and I_{cld} are the observed and bare-cloud (no surface reflection) radiances, respectively. Here we use the so-called mixed Lambertian-Equivalent Reflectivity model to estimate the CRF. In this model, I_{cld} is specified as a Lambertian surface with an equivalent reflectivity of 0.8, and f is set equal to an effective cloud fraction f_{eff} that is derived using the relationship

$$I_{\mathrm{obs}} = f_{\mathrm{eff}} I_{\mathrm{cld}} + (1 - f_{\mathrm{eff}}) I_{\mathrm{clr}}. \tag{3}$$

(e.g., see Stammes et al., 2008, for an overview of the approach that has been used to retrieve the cloud optical centroid pressure at NIR through UV wavelengths). In short, the selection of 0.8 as the cloud reflectivity produces an effective cloud fraction that is generally less than the geometric cloud fraction. Absorption and/or scattering from beneath a thin cloud is accounted for by the second term in Eq. 3. Here, we neglect atmospheric scattering as it is very small at 866 nm. To compute I_{clr}, we use the black-sky 16-day gridded filled-land surface albedo product from Aqua MODIS (MOD43B3) at 865 nm (Lucht et al., 2000). We include only pixels with CRF $<$10% in our sample. High surface albedos over vegetated land and uncertainty in the SCIAMACHY absolute calibration relative to that of MODIS cause this check to allow a large fraction of the

data into our sample, removing only highly clouded pixels. We did not find a significant dependence of F_s on the CRF and more stringent limits on cloud contamination did not significantly alter the derived spatial patterns of F_s.

Owing to uncertainty in the absolute calibration of GOSAT, here we use the cloud fraction derived from the GOSAT CAI. As in Joiner et al. (2011a), we removed pixels with estimated cloud fractions $>$10%. Joiner et al. (2011a) found that this provided similar results to those obtained when the CRF from the Ozone Monitoring Instrument (OMI) onboard the National Aeronautics and Space Administration (NASA) Aura satellite was used for GOSAT cloud detection. Results did not depend substantially on the exact values of the thresholds used here for both GOSAT and SCIAMACY.

4.5 Quality control

To create gridded data sets, we tried different filtering schemes for quality control. For SCIAMACHY, we included all data passing gross quality assurance checks on the filling-in, radiance residuals, and wavelength shifts. We tested whether eliminating the initial scan positions within a nadir-viewing block of observations affected the monthly means. This did not significantly affect the monthly means so all swath positions are included here.

For GOSAT, we tested various filtering methods such as utilitizing consistency between S and P polarizations and radiance residuals. In general, these checks appeared to remove noisy, but good data that was generally helpful in reducing random errors. Therefore, we did not apply any filtering to GOSAT data.

4.6 Scaled fluorescence

When comparing fluorescence with vegetation indices, we use a quantity called "scaled-F" (Joiner et al., 2011a), defined as the retrieved fluorescence F_s divided by $\cos(\mathrm{SZA})$. This scaling roughly accounts for variations in F_s due to the incoming (clear-sky) PAR.

4.7 Uncertainties

Uncertainties for GOSAT retrievals were calculated by Joiner et al. (2011a) assuming only random errors (i.e., instrumental noise). However, errors from unaccounted-for systematic instrumental errors were quite significant. The absolute GOSAT F_s values in this work are smaller (by approximately a factor of 2) than those derived by Joiner et al. (2011a), owing to the new corrections applied.

Because unaccounted-for systematic errors in SCIAMACHY data could be significant and their magnitudes are unknown, it is difficult to quantify the uncertainties in the derived scaled-F. Many SCIAMACHY observations are available for averaging as compared with GOSAT which helps reduce random errors. However, systematic errors are expected to remain. For example, in addition to residual errors left over from imperfect corrections, the South Atlantic anomaly (SAA) has been known to affect measurements over South America. Here, we provide standard errors and standard deviations for gridbox averages to indicate subgridbox variability. We note that there may still be significant errors in the derived absolute values of F_s and scaled-F.

5 Results and Discussion

5.1 Spatial variations in fluorescence

Figure 8 shows retrieved gridded monthly mean scaled-F for July and December 2009 derived from GOSAT at 770 nm and 758 nm (0.696*758 nm + 770 nm) and from SCIAMACHY at 866 nm. The values from SCIAMACHY at 866 nm are significantly smaller than those at 770 nm, as expected. The expected seasonal variation in scaled-F is seen by both sensors, namely, higher Northern Hemisphere terrestrial activity in July versus higher activity in the Southern Hemisphere in December. Like the EVI, the retrieved scaled-F is sensitive to the amount of green biomass contained within the sensor field-of-view or fractional amount of intercepted PAR. Similar patterns are shown in scaled-F by both SCIAMACHY and GOSAT, such as low values over central Brazil in

July and over the northeast of Brazil in December.

Subtle differences in spatial variations are shown between GOSAT- and SCIAMACHY–derived scaled-F. SCIAMACHY shows somewhat less fluorescence at high northern latitudes in the boreal summer as compared with tropical regions. There could be several reasons for this. Firstly, there may be remaining errors due to instrumental effects. Secondly, SCIAMACHY and GOSAT observations are made at different local times; SCIAMACHY observations are made near 10:00 while those of GOSAT are made about 2.5 hours later, just after noon. The shapes of the fluorescence spectra may differ for different types of vegetation as well as different magnitudes and spectral shapes of the incoming solar light. For example, more UV light is absorbed in relatively clear skies at the surface in the tropics where total column ozone and SZAs are low. Plants at these latitudes have more photo-protective mechanisms in place that may produce different fluorescent spectral responses. Compounds within the vegetation besides chlorophyll-a may also contribute to the observed fluorescence. Finally, canopy structure may influence the fluorescence spectra. Multiple scattering within a deep canopy may enhance fluorescence, producing a different spectral response than a sparse canopy (Rosema et al., 1991).

Figures 9-10 show a monthly climatology of fluorescence derived from over 8 years of SCIAMACHY data (January 2003–July 2011) gridded at $0.5^\circ \times 0.5^\circ$ resolution and a similarly gridded climatology of EVI from Aqua MODIS for comparison. An animated version of the climatology is available in the supplemental material. The general patterns from SCIAMACHY are consistent with fluorescence related to vegetation. Interesting differences between scaled-F and EVI are shown clearly here as well as in Fig. 8 including moderate values of EVI over parts of the northeast and southeast US, Europe, and southeast Asia year in the late autumn through early spring when scaled-F is close to zero. The values of scaled-F are more distinctly lower over parts of east and northeast Brazil from May through November as compared with the EVI. Scaled-F also falls within the moderate range for larger areas of Australia than EVI during its summer months (November–February). These differences are further explored in the next

subsection. Note that we show scaled-F here for solar zenith angles up to 80°. In the winter hemisphere at the highest latitudes shown, scaled-F is likely to be overestimated owing to RRS that is not fully accounted for.

5.2 Seasonal variations in fluorescence and EVI

In Fig. 12, we examine the climatological seasonal cycle of fluorescence over several geographic regions shown in Fig. 11. Within each region of interest, we further stratify the data based on the dominant International Geosphere Biosphere Programme (IGBP) land cover class. We show examples for several different biome types, using the same scales in all panels to highlight differences between scaled-F and EVI for the different regions and vegetation types.

Over the pine forests in the southeast US (Fig. 12, panel 1), there is little lag between fluorescence and EVI. Deciduous and mixed forests over the southeast US showed patterns similar to those of evergreen needleleaf with little lag of the EVI (not shown). For this and for many other moderate to high latitude regions, values of the EVI reach minima between 0.2 and 0.3 during winter months, while scale-F is essentially zero. The one exception is southwestern Australia croplands (panel 8), where the EVI reaches a minimum value near 0.1.

Closed shrubland over northeast Brazil (not shown) exhibited a seasonal cycle very similar to open shrubland (panel 3), though with higher values of both scaled-F and EVI. In the open shrubland, both scaled-F and EVI are low in August through November following the wet season green-up that shows peaks in fluorescence and EVI in April. This contrasts sharply with the more heavily forested areas of the central Amazon (panel 2) at similar latitudes where both the EVI and scaled-F remain relatively high year round.

Scaled-F appears to lead the EVI during the green up periods over croplands in the boxed areas of India and Thailand similar to the initial GOSAT results of Joiner et al. (2011a). There is a slightly earlier peak in scaled-F for near-equatorial Thailand (June) as compared with a later peak in India (July) presumably owing to latitude differences.

The lag in the EVI is also much greater during greenup over India (panel 4) than over Thailand (panel 5). In contrast, there is little seasonal variability in the EVI over forested regions of equatorial Indonesia (panel 6), while the fluorescence shows more variability with a minimum around January.

In the forested parts of eastern Australia (panel 7), we see a clear seasonal cycle in scaled-F with a peak in the months December through February. The EVI shows a weaker seasonal variation. In contrast, the EVI shows a sharp peak in August and September over the croplands of southwest Australia (panel 8) while scaled-F shows much less variation.

Higher northern latitudes typically show more seasonal variation and relatively high magnitudes of EVI in summer as compared with the tropics, while the SCIAMACHY scaled-F results suggest show lower peak magnitudes at these latitudes as compared with the tropics. An example is shown over areas of mixed forests and grass in France (panel 9). It is not known whether the relatively low scaled-F values obtained in the norther latitude summer are the result of remaining instrumental bias or represent a biophysical feature.

The savannas of Africa (panels 10,11) show distinct seasonal cycles in both scaled-F and EVI. Again, scaled-F appears to lead the EVI, during both green–up and brown–down periods. The amount of lag varies with region.

Finally, we show an example of deciduous broadleaf in the southern hemisphere (Bolivia, panel 12). Here again we see strong seasonal cycles in both scaled-F and EVI with a slight lag in the EVI during green–up. This region contains a wide variety of biome types. In this region, we also examined areas primarily consisting of open shrubland and grasslands (not shown). In these areas, we found very low (near zero) values of scaled-F as well as low values of EVI ($\sim$0.1–0.2), sharply contrasting with the areas primarily covered by deciduous and evergreen (also not shown, but similar to deciduous) broadleaf vegetation.

The apparent lags of EVI behind the fluorescence signal in several of our examples may have an alternative interpretation related to the fluorescence quantum yield that

is affected by environmentally-induced stress and other factors. The combination of F_s and EVI (or the related parameter fraction absorbed PAR or FPAR) may enable partitioning of ecosystems for the purpose of improving monthly global GPP estimates. An additional measurement of F_s in the 680 nm fluorescence feature may further aid in this partitioning.

5.3 Unexplained filling-in (not due to vegetation fluorescence)

Figure 13 shows a similarly derived monthly climatology of reflectivity at 866 nm. Taken in conjunction with Figs. 9 and 10, this indicates that fluorescence is loosely correlated with reflectivity in vegetated areas as would be expected if the filling-in of the Ca II line has a biogenic source. However, there are also areas of high reflectance with low fluorescence such as over the Sahara and parts of the Saudi Arabian peninsula. This demonstrates that the filling-in is not entirely related to reflectivity as might be the case if the signal was entirely due to an instrumental artifact.

We note a significant filling-in (retrieved as fluorescence) over parts of the Sahara desert (most apparent in May–September) and the Saudi Arabian peninsula where vegetation is sparse and a significant signal from chlorophyll is not expected. These signals sometimes, but not always, occur over very high albedo surfaces. Examination of residual filling-in over Greenland shows residual filling-in over only the brightest area that may not have been well characterized by the cloudy spectra. Cloudy spectra with high radiance values occur primarily in deep and frontal convection where cloud pressures are low. This may lead to an underestimation of filling-in from RRS when these spectra are used as a reference.

Filling-in over barren regions may also be produced by luminescent minerals in soil and/or rock. There are many types of minerals with impurities that luminesce when excited by UV and visible light (Gaft et al., 2005). For example, samples of fluorite (CaF_2) containing Nd^{3+} (Neodymium) centers show laser-induced luminescence with peaks at 866 and 795 nm (Gaft et al., 2005). Similarly, Dy^{3+} (Dysprosium) centers give narrow peaks at 765 and 778 nm.

High filling-in/fluorescence values are also frequently seen around continental and island coastlines, particularly on the Eastern edges. No such features are present in the reflectance climatology shown in Fig. 13. These high values may be due to a spatial aliasing effect or some other instrumental artifact such as distortion of the spectral response function in the presence of large radiance gradients within a satellite footprint. However, we observed neither high radiance residuals nor large wavelength shifts that may accompany such an occurrence.

6 Conclusions and ongoing work

Our results indicate that terrestrial fluorescence filling-in of the 866 nm Ca II line can be detected using hyperspectral instruments (spectral resolutions of the order of tenths of a nm) such as SCIAMACHY. Distinct and similar seasonal cycles of fluorescence are retrieved with SCIAMACHY at 866 nm and GOSAT at 770 nm. This finding is important because it suggests that fluorescence information may be retrieved using potentially low-cost air- and space-borne instrumentation with a relatively simple algorithm that does not rely upon complex atmospheric correction. The detected filling-in signals presumably originate primarily from chlorophyll-a in vegetation though other compounds in vegetation may contribute. In addition to rotational-Raman scattering, luminescent minerals in soil and/or rock may also contribute to red and far-red solar Fraunhofer line filling.

Owing to the large number of observations collected over more than 8 years of operation, SCIAMACHY data can be averaged to provide climatological spatial patterns of fluorescence at a higher resolution than is possible with the current set of GOSAT observations, even though the intrinsic pixel spatial resolution of SCIAMACHY is lower than that of GOSAT. The derived spatial patterns and seasonal cycles in fluorescence are similar to those of the MODIS EVI. However, important differences between scaled-F and EVI are noted. For example, fluorescence appears to lead EVI during greenup and brown down periods in some regions and for some vegetation types similar to re-

sults obtained previously by Joiner et al. (2011a) from GOSAT. A more distinct shut-off of activity in winter and dry months is shown in fluorescence in some areas as compared with EVI.

More work needs to be done to further refine fluorescence retrievals from satellite instruments that were not designed to measure small Fraunhofer line filling-in signals. Owing to the extremely small fluorescence signal measured with instruments that have relatively large systematic errors, our reported absolute values and temporal/spatial variations may still contain residual errors. However, the approach we developed appears to be capable of detecting and correcting for complex, time-varying instrumental artifacts.

The influences of canopy structure and other large-scale parameters, such as chlorophyll content, need to be further investigated in order to understand their effect on large-pixel satellite-retrieved fluorescence (e.g. Rosema et al., 1991; Louis et al., 2005; Meroni and Colombo, 2006; Middleton et al., 2008; van der Tol et al., 2009; Zarco-Tejada et al., 2009; Rascher et al., 2009; Damm et al., 2010). Indeed, it has been suggested that when vegetation is not under stress and the variations in fluorescence yield are small, fluorescence flux from the 740nm emission feature, that is not affected by reabsorption, contains direct information about absorbed PAR (Moya et al., 2004). In addition, the ratio of fluorescence from the 740 and 680 nm features expresses information about chlorophyll concentration (e.g., Gitelson et al., 1999; Saito et al., 1998; Louis et al., 2005). Therefore, additional measurements of fluorescence at other wavelengths will be useful for disentangling the yield information from the chlorophyll content. In order to more fully exploit satellite-derived fluorescence measurements for deriving relationships with key carbon-related parameters such as gross primary production (GPP) or light-use efficiency (LUE), they should be combined with other observable quantities such as the reflectance-based vegetation indices including the PRI. Additional laboratory and field measurements of fluorescence and reflectance spectra for a variety of vegetation types, canopy structures, illumination, and environmental conditions will help to improve the interpretation and use of satellite-derived fluores-

cence information.

The upcoming launch of the Orbiting Carbon Observatory-2 (OCO-2) (Crisp et al., 2004) will facilitate the use of solar Fraunhofer lines for fluorescence retrievals at similar wavelengths near the O_2-A band (Frankenberg et al., 2011a) and provide more opportunities for fluorescence measurements. The FLuorescence EXplorer (FLEX) (Rascher, 2007; European Space Agency, 2008), an ESA Explorer Mission selected for Phase A/B1 in early 2011, plans to utilize the O_2-A and B bands for chlorophyll fluorescence retrievals (Guanter et al., 2010). FLEX would provide fluorescence information at a higher spatial resolution than current satellite sensors that are able to measure fluorescence but were not designed and optimized for that purpose.

Acknowledgements. Funding for this work was provided by the NASA Carbon Cycle Science program (NNH10DA001N) managed by Drs. Diane E. Wickland and Richard Eckman. The authors are indebted to C. Retschler for assistance with the satellite data sets, particularly the SCIAMACHY data. We gratefully acknowledge the European Space Agency, the GOSAT project, and the MODIS data processing team for making available the SCIAMACHY, GOSAT, and MODIS data, respectively, used here. We also thank W. Philpot, W. Cook, K. F. Huemmrich, Y.-B. Cheng, J. Mao, C. Weaver, D. Crisp, and A. da Silva for helpful discussions.

Appendix A Instrumental effects in SCIAMACHY data that may produce false filling-in

A1 Memory effect

In channels 1-5, it was found that the signal deviates from a linear response. The deviation depends upon the signal level of the previous readout. It also depends on the signal level including analog offset and dark current. Since there is a dependence on the previous signal for a large range of detector fillings, artificial spectral features can be introduced into the measurements.

We found systematic biases in Fraunhofer line filling as a function of position within a block of nadir measurements. The first several positions (following the limb-viewing mode) have the largest biases. Because of repeating orbital patterns, if this effect is not accounted for, a cross-track striping will be present in the observed filling-in, even after averaging a month of data.

A2 Dark current

There are two components that contribute to the dark signal in channels 1-5: the analog offset and the leakage current. The former does not depend on integration time while the latter does. We found different biases in the filling-in for the two primary pixel exposure times (PETs) used for nadir measurements in channels 4 and 5 that may be a result of unaccounted for dark signals.

A3 Wavelength calibration and undersampling

Due to the Doppler and other effects, there are small wavelength shifts in Earth spectra with respect to the measured solar spectra. We found that these wavelength shifts vary systematically with latitude. Wavelength shifts between observed and reference spectra must be accurately accounted for when deriving a relatively small filling-in signal.

A4 Straylight

Stray light may be classified as two types: spectral and spatial. Both of these can distort observed spectra. Spatial stray light mainly affects the limb measurements of SCIAMACHY, but may also produce errors in a fluorescence retrieval in the nadir mode. Spectral stray light may be caused by diffuse reflection that adds signal to all detector pixels in a given channel, thus mimicking fluorescence. The largest expected uniform stray light fraction in SCIAMACHY is 0.14% (Lichtenberg et al., 2006).

So-called "ghost" stray light is caused by reflection from one wavelength to another. It does not add signal to all pixels equally, but can distort the spectrum. The correction

method is accurate to around 25%, leaving at most 1% stray light in the spectrum.

A5 Calibration

Various issues with SCIAMACHY's radiometric calibration are discussed by Lichtenberg et al. (2006). These may affect the absolute values of derived fluorescence. In addition to radiometry, the applied calibration scheme may introduce spectral features and thus produce false filling-in.

References

Amoros-Lopez, J., Gomez-Chova, L., Vila-Frances, J., Alonso, L., Calpe, J., Moreno, J., and del Valle-Tascon, S.: Evaluation of remote sensing of vegetation fluorescence by the analysis of diurnal cycles, Intl. J. Remote Sens., 29, 5423-5436, 2008.

Bovensmann, H., Burrows, J. P., Buchwitz, M., Frerick, J., Noel, S., Rozanov, V. V., Chance, K. V., and Goede, A. (1999). SCIAMACHY mission objectives and measurement modes, J. Atmos. Sci., 56, 127–150.

Burrows J., Vountas, M., Hang, H., Chance, K., Marquard, L., Muirhead, K., Platt, U., Richter, A., and Rozanov, V.: Study of the Ring effect, ESA final report, 1996.

Campbell, P. K. E., Middleton, E. M., Corp, L. A., and Kim, M. S.: Contribution of chlorophyll fluorescence to the apparent vegetation reflectance, Sci. Total Environ., 404, 433–439, 2008.

Chance, K. V. and Spurr, R. J. D.: Ring effect studies: Rayleigh scattering, including molecular parameters for rotational Raman scattering, and the Fraunhofer spectrum, Appl. Opt., 36, 5224-5230, 1997.

Chance, K., Kurosu, T. P., and Sioris, C. E.: Undersampling correction for array detector-based satellite spectrometers, Appl. Optics, 44, 1296–1304, 2005.

Chance, K. and Kurucz, R. L.: An improved high-resolution solar reference spectrum for Earth's atmosphere measurements in the ultraviolet, visible, and near infrared, J. Quant. Spectrosc. Radiat. Trans., 111, 1289–1295, 2010.

Chappelle, E. W., Wood, F. M., McMurtrey, J. E., and Newcomb, W. W.: Laser-induced fluorescence of green plants. 1: A technique for the remote detection of plant stress and species differentiation, Appl. Opt., 23, 134–138, 1984.

Chappelle, E. W. and Williams, D. L., Laser-induced fluorescence (LIF) from plant foliage, IEEE Trans. Geosci. Remote Sens., GE-25, 726–736.

Corp, L.A., McMurtrey, J. E., Middleton, E. M., Mulchi, C. L., Chappelle, E. W., and Daughtry, C. S. T.: Fluorescence Sensing Systems: In vivo detection of biophysical variations in field corn due to nitrogen supply, Remote Sens. Environ., 86, 470–479, 2003.

Corp, L. A., Middleton, E. M., McMurtrey, J. E., Campbell, P. K. E., and Butcher, L. M.: Fluorescence sensing techniques for vegetation assessment, Appl. Opt., 45, 1023–1033, 2006.

Crisp, D.: The Orbiting Carbon Observatory (OCO) mission, Adv. in Space Res., 34, 700–709, 2004.

Damm, A., Elbers, J., Erler, A., et al.: Remote sensing of sun-induced fluorescence to improve modeling of diurnal courses of gross primary production (GPP), Global Change Biology, 16, 171–186, doi:10.1111/j.1365-2486.200901908.x, 2010.

Danichkin, S. A., Eliseev, A .A., Popova, T. N., Ravodina, O. V. and Stenina, V. V.: Raman scattering parameters for gas molecules (Review), J. Appl. Spectrosc., 35,1057-1066, 1982.

Deutsches Zentrum fur Luft- und Raumfahrt: SCIAMACHY Level 1b-1c processing The SciaL1c Command-line tool software user's manual, ENV-SUM-DLR-SCIA-0071, Issue 6.0, 2006.

Edner, H., Johansson, J., Svanberg, S., and Wallinder, E.: Fluorescence lidar multicolor imaging of vegetation, Appl. Opt., 33, 2471–2479, 1994.

European Space Agency:. ESA SP-1313/4 Candidate Earth Explorer Core Missions - Reports for Assessment: FLEX – FLuorescence EXplorer, published by ESA Communication Production Office, Noordwijk, The Netherlands, http://esamultimedia.esa.int/docs/SP1313-4_FLEX.pdf., 2008.

Fenner W. R., Hyatt, H. A., Kellam, J. M., and Porto, S. P. S.: Raman cross section of some simple gases, J. Opt. Soc. America, 63, 73-77, 1973.

Flexas, J., Escalona, J. M., Evain, S., J. Gulías, Moya, I., Osmond, C. B., and Medrano, H.: Steady-state chlorophyll fluorescence (Fs) measurements as a tool to follow variations of net CO_2 assimilation and stomatal conductance during water-stress in C_3 plants, Physiologia Plantarum, 114, 231–240, 2002.

Frankenberg, C., Butz, A., and Toon, G. C.: Disentangling chlorophyll fluorescence from atmospheric scattering effects in O2A-band spectra of reflected sun-light, Geophys. Res. Lett., 38, L03801, doi:10.1029/2010GL045896, 2011.

Frankenberg, C., Fisher, J. B., Worden, J., Badgley, G., Saatchi, S. S., Lee, J.-E., Toon, G. C.,

Butz, A., Jung, M., Kuze, A., and Yokota, T.: New global observations of the terrestrial carbon cycle from GOSAT: Patterns of plant fluorescence with gross primary productivity, Geophys. Res. Lett., 38, L17706, doi:10.1029/2011GL048738, 2011.

Gaft, M., Reisfeld, R., and Panczer, G.: Modern luminescence spectroscopy of minerals and materials, Spring-Verlag, Berlin, Heidelberg, 356 pp., 2005.

Gitelson, A. A., Buschmann, C., and Lichtenthaler, H. K.: The chlorophyll fluorescence ratio F_{735}/F_{700} as an accurate measure of chlorophyll content in plants, Remote Sens. Environ., 69, 296–302, 1999.

M. Gottwald, H. Bovensmann, G. Lichtenberg, S. Noel, A. von Bargen, S. Slijkhuis, A. Piters, R. Hoogeveen, C. von Savigny, M. Buchwitz, A. Kokhanovsky, A. Richter, A. Rozanov, T. Holzer-Popp, K. Bramstedt, J.-C. Lambert, J. Skupin, F. Wittrock, H. Schrijver, and Burrows, J. P.: SCIAMACHY, Monitoring the Changing Earth's Atmosphere, Published by DLR and Springer, doi 10.1007/978-90-481-9896-2, 2006.

Guanter, L., Alonso, L., Gómez-Chova, L., Amorós-López, J., Vila-Francés, J., and Moreno, J.: Estimation of solar-induced vegetation fluorescence from space measurements, Geophys. Res. Lett., doi:10.1029/2007GL029289, 2007.

Guanter, L., Alonso, L., Gómez-Chova, Meroni, M., Preusker, R., Fischer, J., and Moreno, J.: Developments for vegetation fluorescence retrieval from spaceborne high-resolution spectrometry in the O_2-A and O_2-B absorption bands, J. Geophys. Res., 115, D19303, doi:10.1029/2009JD013716, 2010.

Heise, H. M. and Schrotter, H. W.: Rotation-vibration spectra of gases, Infrared and raman Spectroscopy, Methods and Applications, VCH, Weinheim, Chapt. 4.3, 253-297, 1995.

Hemphill, W. R., and Vickers, R.: Geological studies of the Earth and planetary surfaces of ultraviolet absorption and stimulated luminescence, NASA Tech. Lett. NASA-33, Washington, DC, USA, 1966.

Hemphill, W. R., Tyson, R. M., Theisen, A. F.: Spectral luminescence properties of natural specimens in the scheelite-powellite series, and an assessment of their detectivity with an airborne Fraunhofer line discriminator, Economic Geology, 83, 637-646, 1988.

Huete, A. R., Didan, K., Miura, T., Rodriguez, E. P., Gao, X., Ferreira, L. G.: Overview of the radiometric and biophysical performance of the MODIS vegetation indices, Remote Sens. Environ., 83, 195–213, 2002.

Huete, A. R., Didan, K., Shimabukuro, Y. E., Ratana, P., and Saleska, S. R.: Amazon rainforests green-up with sunlight in dry season, Geophys. Res. Lett., 33, L06405,

doi:10.1029/2005GL025583, 2006.
Joiner, J., Yoshida, Y., Vasilkov, A. P., Yoshida, Y., Corp, L. A., and Middleton, E. M.: First observations of global and seasonal terrestrial chlorophyll fluorescence from space, Biogeosci., 8, 637-651, doi:10.5194/bg-8-637-2011, 2011.
Joiner, J., Vasilkov, A. P., Gupta, P., Bhartia, P. K., Veefkind, P., Sneep, M., de Haan, J., Polonsky, I., and Spurr, R.: Fast simulators for satellite cloud optical centroid pressure retrievals, 1. Evaluation of OMI cloud retrievals, Atmos. Meas. Tech. Disc., 6185-6228, doi:10.5194/amtd-4-6185-2011, 2011.
Kuze, A., Suto, H., Nakajima, M., and Hamazaki, T.: Thermal and near infrared sensor for carbon observation Fourier-transform spectrometer on the Greenhouse Gases Observing Satellite for greenhouse gases monitoring, Appl. Opt., 48, 6716–6733, 2009.
Kuze, A., OBrien, D. M., Taylor, T. E. , Day, J. O, ODell, C., Kataoka, F., Yoshida, M., Mitomi, Y., Bruegge, C., Pollock, H., Basilio, R., Helmlinger, M., Matsunaga, T., S. Kawakami, S., Shiomi, K., Urabe, T. and Suto H.: Vicarious calibration of the GOSAT sensors using the Railroad Valley desert playa, IEEE Trans. Geosci. Remote Sens., doi: 10.1109/TGRS.2010.2089527, 2011.
Kuze, A., Suto, H., Shiomi, K., Nakajima, M.: GOSAT TANSO calibration and characterization of 2 years on orbit operation, 2011.
Lichtenberg, G., Kleipool, Q., Krijger, J. M., van Soest, G., van Hees, R., Tilstra, L. G., Acarreta, J. R., Aben, I., Ahlers, B., Bovensmann, H., Chance, K., Gloudemans, A. M. S., Hoogeveen, R. W. M., Jongma, R. T. N., Noel, S., Piters, A., Schrijver, H., Schrijvers, C., Sioris, C. E., Skupin, J., Slijkhuis, S., Stammes, P., and Wuttke, M.: SCIAMACHY level 1 data: calibration concept and in-flight calibration, Atmos. Chem. Phys., 6, 5347–5367, 2006.
Louis, J., Ounis, A., Ducruet, J.-M., Evain, S., Laurila, T., Thum, T., Aurela, M., Wingsle, G., Alonso, L., Pedros, R., and Moya, I.: Remote sensing of sunlight-induced chlorophyll fluorescence and reflectance of Scots pine in the boreal forest during spring recovery, Remote Sens. Environ., 96, 37–48, 2005.
Lucht, W., Schaaf, C. B., and Strahler, A. H.: An Algorithm for the retrieval of albedo from space using semiempirical BRDF models, IEEE Trans. Geosci. Remote Sens., 38, 977–998, 2000.
McFarlane, J. C., Watson, R. D., Theisen, A. F., Jackson, R. D., Ehrler, W. L., Pinter, P. J., Idso, S. B., and Reginato, R. J.: Plant stress detection by remote measurement of fluorescence, Appl. Opt., 19, 3287–3289, 1980.
Meroni, M. and Colombo, R.: Leaf level detection of solar induced chlorophyll fluorescence

by means of a subnanometer resolution spectroradiometer, Remote Sens. Environ., 103, 438–448, 2006.

Meroni, M., Picchi, V., Rossini, M., Cogliati, S., Panigada, C., Nali, C., Lorenzini, G., Colombo, R.: Leaf level early assessment of ozone injuries by passive fluorescence and photochemical reflectance index, Intl. J. Remote Sens., 29, 5409–5422, 2008.

Meroni, M., Rossini, M., Guanter, L., Alonso, L., Rascher, U., Colombo, R., and Moreno, J.: Remote sensing of solar-induced chlorophyll fluorescence: Review of methods and applications, Remote Sens. Environ., 113, 2037–2051, 2009.

Middleton, E. M., Corp, L. A., and Campbell, P. K. E.: Comparison of measurements and FluorMOD simulations for solar induced chlorophyll fluorescence and reflectance of a corn crop under nitrogen treatments, Intl. J. Rem. Sensing, Special Issue for the Second International Symposium on Recent Advances in Quantitative Remote Sensing (RAQRSII), 29, 5,193–5,213, 2008.

Middleton, E. M., Cheng, Y.-B., Corp, L. A., Huemmrich, K. F., Campbell, P. K. E. Zhang, Q.-Y., Kustas, W. P. and Russ, A. L.: Diurnal and seasonal dynamics of canopy-level solar-induced chlorophyll fluorescence and spectral reflectance indices in a cornfield, Proc. 6th EARSeL SIG Workshop on Imaging Spectroscopy, CD-Rom, 12 pp., Tel-Aviv, Israel March 16-19, 2009.

Moya I., Camenen, L. Evain, S. et al.: A new instrument for passive remote sensing : 1. Measurements of sunlight-induced chlorophyll fluorescence. Remote Sens. Environ., 91, 186–197, 2004.

Plascyk, J. A., and Gabriel, F. C.: The Fraunhofer Line Discriminator MKII – An airborne instrument for precise and standardized ecological luminescence measurement, IEEE Trans. Instrum. Meas., 24, 1975.

Rascher, U.: FLEX – Fluorescence Explorer: A remote sensing approach to quatify spatio-temporal variations of photosynthetic efficiency from space, Photosynth. Res., 91, 293–294, 2007.

Rascher, U., I. Agati, L. Alonso, et al.: CEFLES2: the remote sensing component to quantify photosynthetic efficiency from the leaf to the region by measuring sun-induced fluorescence in the oxygen absorption bands. Biogeosci., 6, 1181–1198, 2009.

Rosema, A., Verhoef, W., Schoote, J., and Snel, J. F. H.: Simulating fluorescence light-canopy interaction in support of laser-induced fluorescence measurements, Rem. Sens. Env., 37, 117–130, 1991.

Saito, Y., Kanoh, M., Hatake, K., Kawahara, T. D., and Nomura, A.: Investigation of laser-induced fluorescence of several natural leaves for application to lidar vegetation monitoring, Appl. Opt., 37, 431–437, 1998.

Sioris, C., Courrèges-Lacoste, G. B. and Stoll M. P.: Filling in of Fraunhofer lines by plant fluorescence: Simulations for a nadir-viewing satellite-borne instrument. Geophys. Res. Lett., 108, 4133, doi:10.1029/2001JD001321, 2003.

Spurr, R. J. D., de Haan, J., van Oss, R., and Vasilkov, A. P.: Discrete ordinate radiative transfer in a stratified medium with first order rotational Raman scattering, J. Quant. Spectrosc. Ra., 109, 404425, 2008.

Stacy, J. E., Breckinridge, J. B., Conel, J. E., and Chrisp, M. P.: Orbital Fraunhofer line discriminator feasibility study, Jet Propulsion Laboratory report D-1512, NASA FOIA Request No. 10-JPL-F-01288, 1984.

Stammes, P., Sneep, M., de Haan, J. F., Veefkind, J. P., Wang, P., and Levelt, P. F.: Effective cloud fractions from the Ozone Monitoring Instrument: Theoretical framework and validation, J. Geophys. Res., 113, D16S38, doi:10.1029/2007JD008820, 2008.

Thuillier, G., Hersé, M., Labs, D., Foujols, T., Peetermans, W., Gillotay, D., Simon, P. C., and Mandel, H.: The solar spectral irradiance from 200 to 2400 nm as measured by the SOLSPEC spectrometer from the ATLAS and EURECA missions, Solar Phys., 214, 122, 2003.

Thuillier, G., Floyd, L., Woods, T.N., Cebula, R., Hilsenrath, E., Hersé, M., and Labs D.: Solar irradiance reference spectra, in: Pap, J., Fox, P., Frohlich, C., Hudson, H.S., Kuhn, J., McCormack, J., North, G., Sprigg, W., Wu, S.T. (Eds.), Solar Variability and its Effect on the Earths Atmosphere and Climate System, Geophysical Monograph, vol. 141, American Geophysical Union, Washington, DC, pp. 171194, 2004.

van der Tol, C., Verhoef, W., and Rosema, A.: A model for chlorophyll fluorescence and photosynthesis at leaf scale, Agricult. Forest Meteorol., 149, 96–105, 2009.

Vasilkov, A. P., Joiner, J., Gleason, J. F., and Bhartia, P. K.: Ocean Raman scattering in satellite backscatter ultraviolet measurements, Geophys. Res. Lett., 29, 1837-1840, 2002.

Watson, R. D.: Airborne Fraunhofer line discriminator surveys in southern California, Nevada, and central New Mexico, Workshop of applications of luminescence techniques to Earth resource studies. A Lunar and Planetary Institute Workshop Dec. 10-12, 1980, in Houston, TX, USA. Ed. Hemphill, W. R. and Settle, M., Tech Rep. 81-03, LPI, Houston, TX., 28–35, 1981.

Xu, L., Samanta, A., Costa, M. H., Ganguly, S., Nemani, R. R., and Myneni, R. B.: Widespread

decline in greenness of Amazonian vegetation due to the 2010 drought, Geophys. Res. Lett., 38, L07402, doi:10.1029/2011GL046824, 2011.

Yokota, T., Yoshida, Y., Eguchi, N., Ota, Y., Tanaka, T., Watanabe, H., and Maksyutov, S.: Global Concentrations of CO_2 and CH_4 Retrieved from GOSAT: First Preliminary Results, Sci. Online Lett. Atm., 5, 160–163, 2009.

Zarco-Tejada, P. J., Berni, J. A. J., Suarez, L., Sepulcre-Cantó, G., Morales, F., and Miller, J. R.: Imaging chlorophyll fluorescence with an airborne narrow-band multispectral camera for vegetation stress detection, Remote Sens. Environ., 113, 1262–1275, 2009.

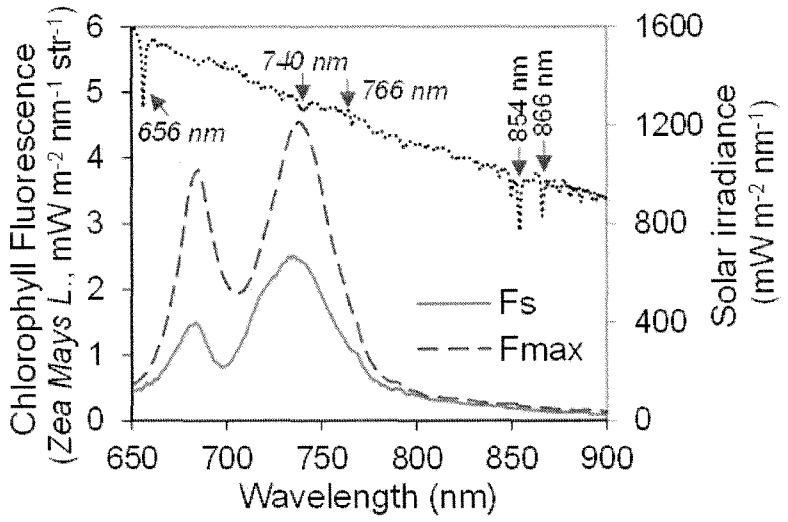

Fig. 1. Measured fluorescence spectra of excised corn leaves (Zea Mays L.) in the laboratory, with simulated solar illumination at full mid-day sun intensity as measured below a long-pass filter blocking wavelengths longer than 665 nm, showing maximum fluorescence (F_{max}) after 5 min. of dark adaptation, steady state fluorescence (F_s, achieved in less than 0.5 minute after illumination), and a sample solar spectrum from Thuillier et al. (2003, 2004) (1 nm spectral resolution).

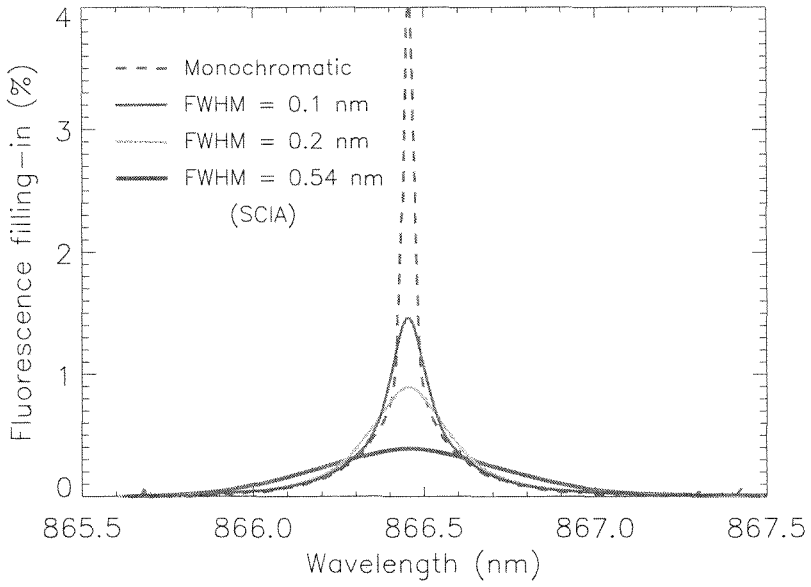

Fig. 2. Simulated spectral filling-in around the Ca II solar line from fluorescence=0.2 mW/m^2/sr/nm, SZA=40°, nadir, and surface albedo=0.3 (RRS not included) for different instrument resolutions (triangular slit function) with full-width half-maximum (FWHM) as indicated including that of SCIAMACHY (SCIA).

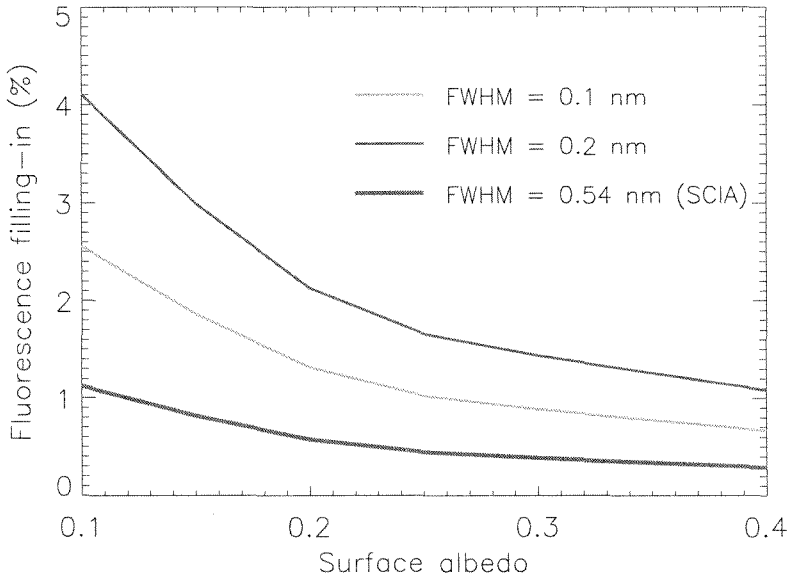

Fig. 3. Filling-in due to fluorescence=0.2 mW/m^2/nm/sr, SZA=20°, and nadir as a function of surface albedo for different instrument spectral resolutions.

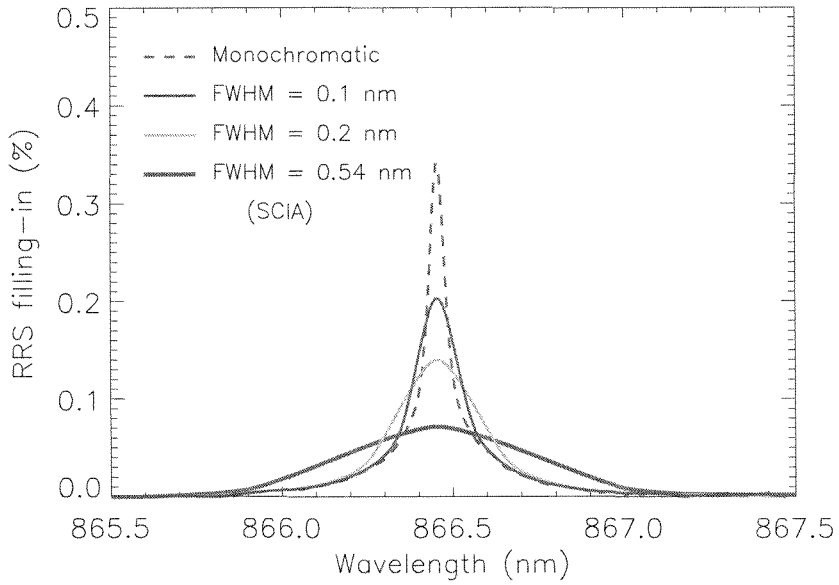

Fig. 4. Simulated filling-in spectra due to rotational-Raman scattering (RRS) only at SZA=40°, nadir, and surface albedo=0.3 for different instrument spectra resolutions.

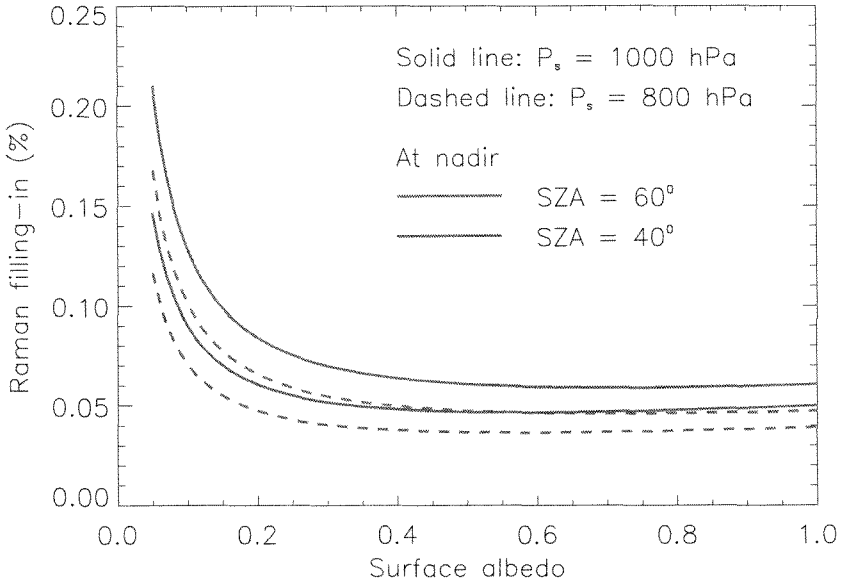

Fig. 5. Filling-in of Ca II line at 866 nm due to rotational-Raman scattering as a function of surface albedo for two solar zenith angles (SZA) and two surface pressures (P_s) showing simulated difference between low clouds over ocean (800 hPa) and a low lying land area (1000 hPa).

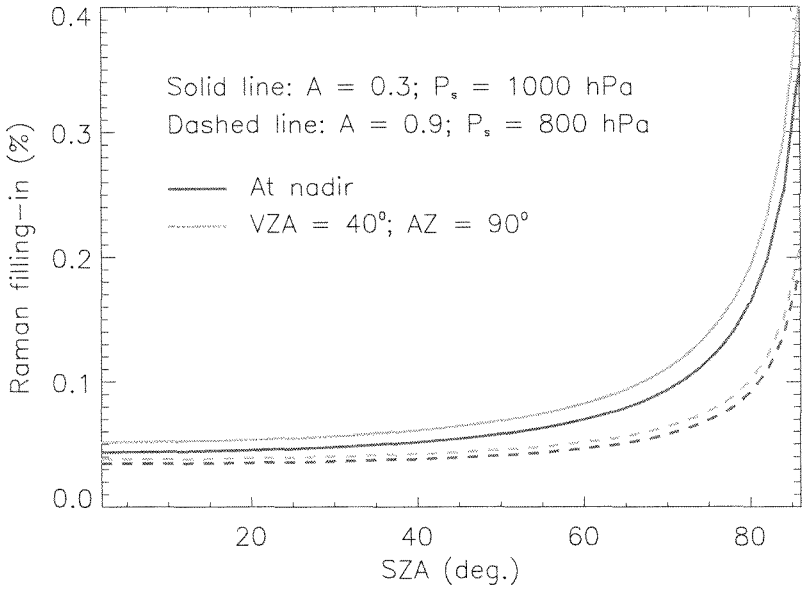

Fig. 6. Filling-in of Ca II line at 866 nm due to rotational-Raman scattering as a function of solar zenith angle for 2 view zenith angles (VZA) typical of minimum (nadir, 0°) and maximum (40°) for SCIAMACHY for a relative azimuth angle (AZ) of 90°.

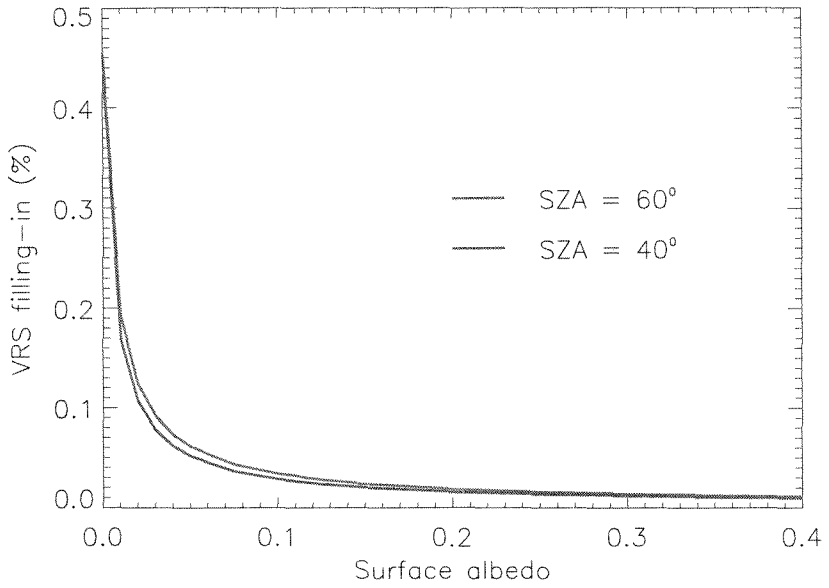

Fig. 7. Filling-in of Ca II line at 866 nm due to vibrational-Raman scattering (VRS) as a function of surface albedo for 2 solar zenith angles (SZA).

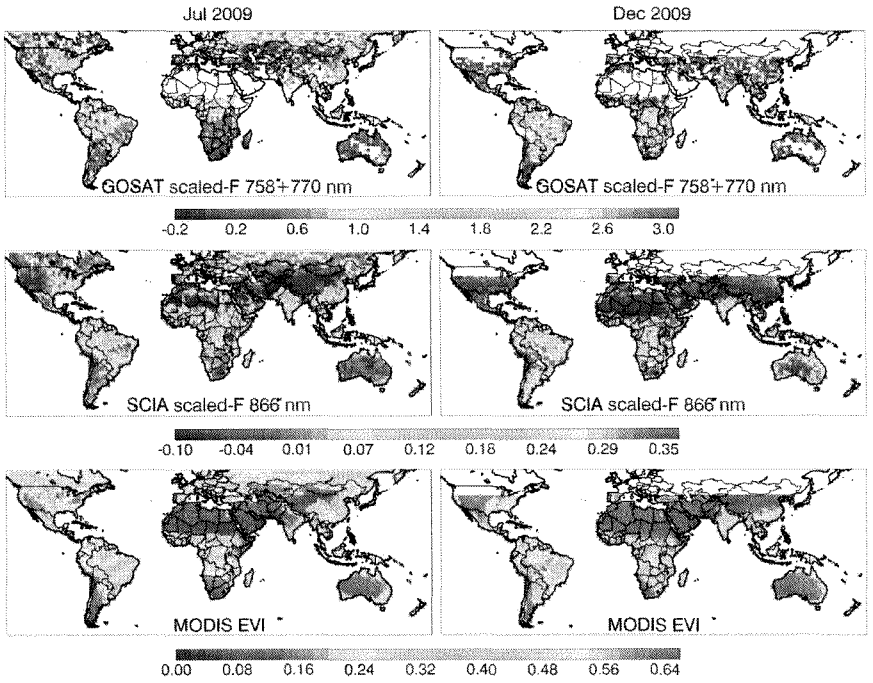

Fig. 8. Derived monthly averages for July (left panels) and December (right panels) 2009; Top: fluorescence scaled by cos(SZA) (scaled-F) (unitless) from GOSAT (0.696*758 nm + 770 nm); Middle: SCIAMACHY 866 nm; Bottom: Aqua MODIS enhanced vegetation index (EVI)

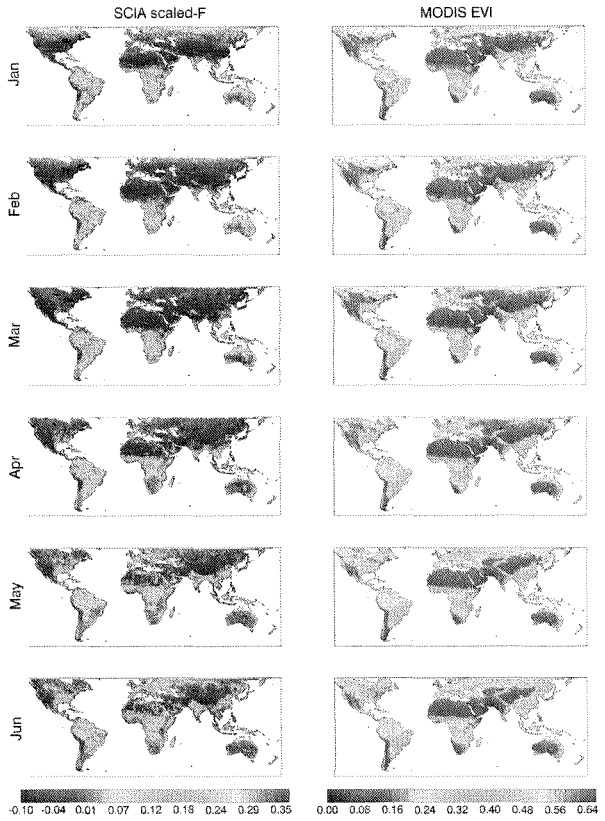

Fig. 9. Monthly mean scaled-F derived from 8+ years of SCIAMACHY data (Jan. 2003 – July 2011) gridded at $0.5^\circ \times 0.5^\circ$ resolution (left) and similarly gridded EVI from Aqua MODIS for January through June (top to bottom).

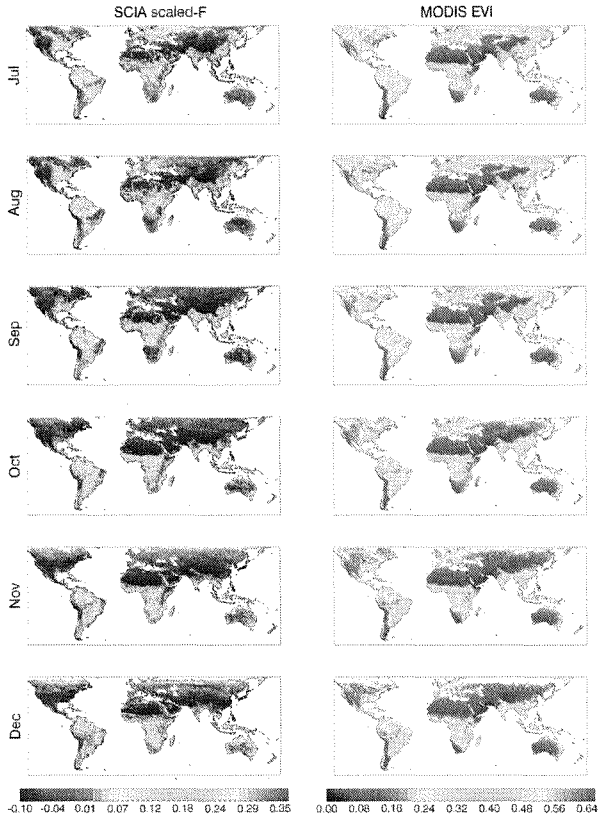

Fig. 10. Similar to Fig. 9 but for July through December derived from 8+ years of SCIAMACHY data (Jan. 2003 – July 2011).

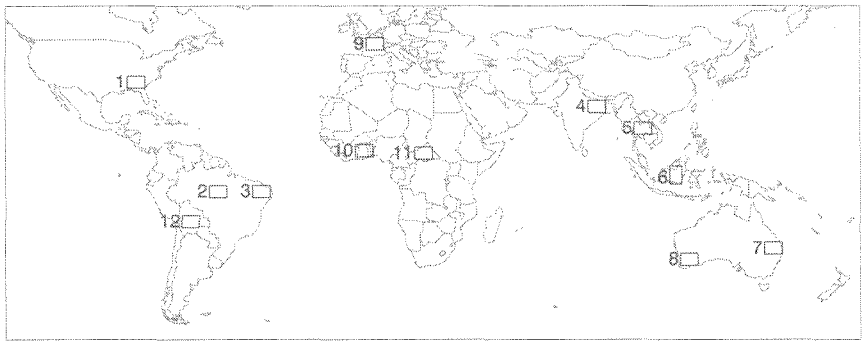

Fig. 11. Regions used for calculating seasonal cycles shown in Fig. 12.

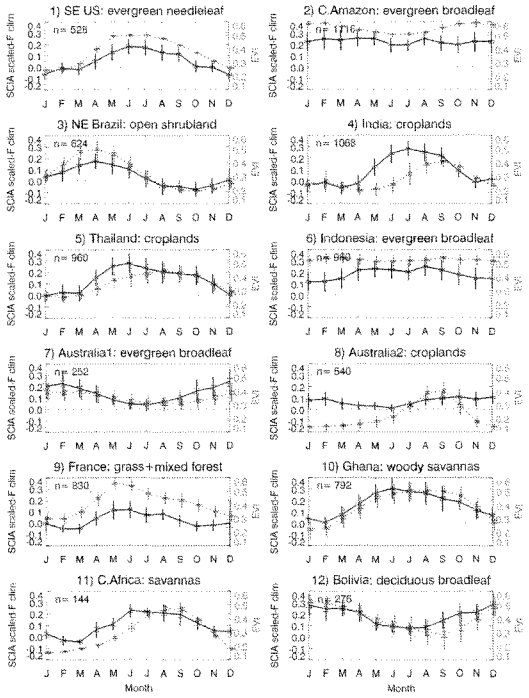

Fig. 12. Seasonal cycles derived for the regions shown in the Fig. 11 map, using $0.5° \times 0.5°$ gridbox monthly means within the region and the vegetation type as listed: Black solid line: scaled-F derived from SCIAMACHY (left axis, unitless) for the regions indicated; Horizontal lines indicate error of the monthly mean; Vertical lines indicate the standard deviation; Green dotted line: MODIS Enhanced Vegetation Index (EVI, right axis, unitless). The numbers indicated are the number of monthly mean gridboxes used in each plot.

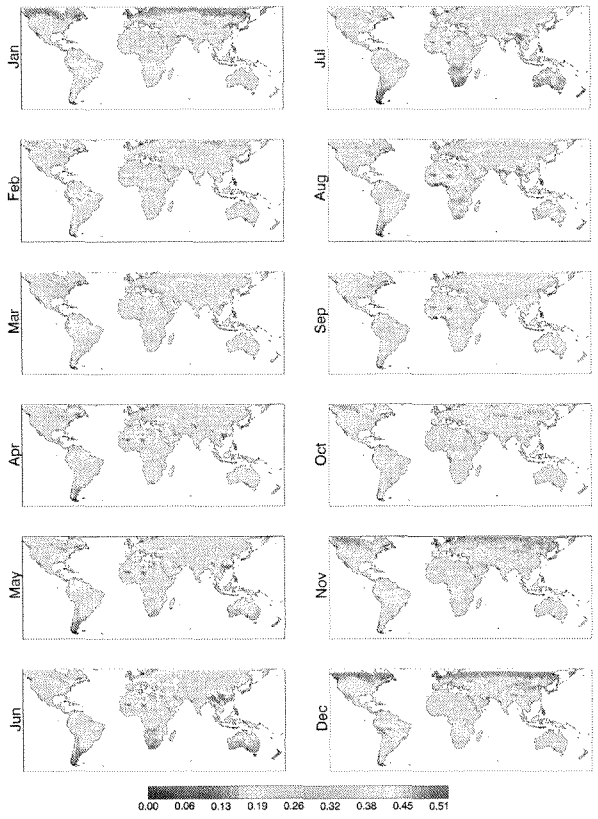

Fig. 13. Monthly mean gridded reflectivity near 866 nm as derived from 8+ years of SCIAMACHY data (Jan. 2003 – July 2011) similar to Fig. 9.